Eur. Phys. J. Plus (2019) **134**: 296
DOI 10.1140/epjp/i2019-12690-2

THE EUROPEAN PHYSICAL JOURNAL PLUS

Regular Article

Simple synthesis, structural and optical properties of cobalt ferrite nanoparticles

A.V. Ravindra[1,2,3,a], M. Chandrika[4], Ch. Rajesh[4,5], Pratap Kollu[6], Shaohua Ju[1,2,3], and S.D. Ramarao[4]

[1] State Key Laboratory of Complex Nonferrous Metal Resources Clean Utilization, Kunming University of Science and Technology, Kunming 650093, Yunnan, China
[2] Key Laboratory of Unconventional Metallurgy, Kunming University of Science and Technology, Kunming 650093, Yunnan, China
[3] Faculty of Metallurgical and Energy Engineering, Kunming University of Science and Technology, Kunming 650093, Yunnan, China
[4] Advanced Functional Materials Research Centre, Department of Physics, Koneru Lakshmiah Education Foundation, Vaddeswaram, Guntur, Andhra Pradesh 522502, India
[5] Department of Physics, GVP College of Engineering (A), Madhurwada, Visakhapatnam 530048, India
[6] Centre for Advanced Studies in Electronics Science and Technology (CASEST), School of Physics, University of Hyderabad, Gachibowli, Hyderabad 500046, India

Received: 20 November 2018 / Revised: 22 March 2019
Published online: 26 June 2019

Abstract. Cobalt ferrite ($CoFe_2O_4$) nanoparticles have been successfully synthesised by simple and economic co-precipitation method at 90 °C for 2 h using a biodegradable surfactant (starch), and by annealing at 500 °C for 1, 2, and 6 h. The XRD patterns reveal spinel $CoFe_2O_4$ phase for as-synthesized and annealed samples without any impurity phase. FTIR spectra also demonstrate the characteristic absorption bands of $CoFe_2O_4$ phase and starch surfactant. SEM images display nearly spherical morphology for all the samples and the average particle size increases when annealed at 500 °C and for prolonged durations at the same temperature. The direct band gap of $CoFe_2O_4$ nanoparticles decreases with increasing particle size and the direct band gap values are attributed to spin-allowed d to d on-site transitions. The PL spectra exhibit peaks associated with transitions of charge carriers to near edge, surface, and defect states. The PLE peaks suffer blue shift when annealed at 500 °C for 1 h and then red shift on further prolonging the annealing time to 2 and 6 h at the same temperature. Such results offer new opportunities for optimizing and enhancing the performance of cobalt ferrite where the optical properties are decisive.

1 Introduction

Spinel ferrites having general formula AB_2O_4, where "A" is a divalent cation and "B" is a trivalent cation, have been of great interest owing to their structure dependent properties and numerous applications [1,2]. In addition, spinel ferrites exhibit extra catalytic sites by virtue of the crystal lattice which enhances the efficiency, and a band gap capable of absorbing the visible light [3]. Cobalt ferrite ($CoFe_2O_4$ (CFO)) with good thermal, chemical, and mechanical stability, and moderate magnetization distinguishes itself among ferrites on account of its wide range of applications in evolution of sensors [4], magnetic recording devices [5], quantum computing [6], microwave shielding [7], magneto-optical devices [8], catalysis [9], drug delivery [10], hyperthermia [11]. The CFO has also been used to fabricate heterostructures for spin filtering [12], resistive switching [13], and magnetoelectric coupling between ferromagnetic and ferroelectric thin film layers [14]. Generally, the CFO has an inverse spinel structure with space group $O_7^h - Fd\bar{3}m$ in which 8 Co^{2+} occupy half of the octahedral (B) sites, 8 Fe^{3+} occupy the rest of octahedral sites, and the 8 Fe^{3+} in tetrahedral (A) sites. However, CFO can be a partial normal spinel, with the tetrahedral sites partially occupied by Co^{2+}, depending on the preparation conditions and annealing temperature [15,16].

Ferrite nanoparticles of different structure and morphology have been synthesized by several methods [2,17]. However, co-precipitation method is often preferred owing to its simplicity, cost effectiveness, easy implementation,

[a] e-mail: ravindra.annavarapu@outlook.com (corresponding author)

control, and yield [18]. Tatarchuk *et al.* highlighted and discussed the significance of influence of various synthesis methods at different environmental conditions, cation and anion distribution, and ion substitution on the structure of the various ferrite nanoparticles. Further, the impact of change in the shape and size of microstructure on the electrical, magnetic, and optical properties of ferrites and consequently their scope in various prominent fields like sensors, microwave, catalytic and biomedical applications was discussed [19]. The influence of various parameters on the magnetic properties of ferrites nanoparticles has been widely studied in the literature [20–22]. The important factor of ferrite structure deciding the properties is the distribution of cations in different sites, which is influenced by the sample synthesis and treatment conditions. In recent times, Abu El-Fadl *et al.* studied the impact of site occupancy of Ni ions on the magnetic properties of single-phase Ni doped zinc ferrite nanoparticles obtained by microwave combustion method. They have observed that with the increase in Ni ions content, the lattice constants and lattice strains decrease whereas the saturation magnetization increases initially and later decreases [23]. Also, Ahmed *et al.* investigated the changes in the concentration of surface donor's and acceptor's active centers due to ionic substitution in Mg-Cu-Zn ferrite obtained by ceramic method by estimating the changes in inversion parameter caused by γ-ray irradiation. They successfully explained the new antistructural modeling for the pristine and irradiated samples to describe the lattice defects and the surface active centers as a function of Mg ion content at different doses of γ irradiation [24].

There have been good number of theoretical studies dedicated to study the electronic structure of CFO. Szotek *et al.* showed that the ground state of bulk CFO to be half-metallic using the self-interaction corrected density functional theory (DFT) calculations [25]. The inverse spinel situation illustrated bulk CFO to be an insulator with a gap of 0.8 eV, while the gap was reduced to 0.21 eV in the normal spinel case. Hou *et al.* demonstrated that bulk CFO in the inverse spinel structure is insulating with a band gap of 0.72 eV using the generalized gradient approximation augmented with an on-site Coulomb repulsion (GGA+U) calculations [26]. At the same time, other theoretical reports predicted a band gap value of 0.63 eV [27] and 0.52 eV [25] for bulk CFO, using local density approximation augmented with an on-site Coulomb repulsion (LDA+U) approximation. On the other hand, there are very few experimental reports on the optical properties of CFO. Tanabe and Sugano observed three distinct low energy peaks centered at ~ 0.75, ~ 1.25, and ~ 1.75 eV in the optical absorption spectra of CFO nanoparticles, which were attributed to spin-allowed Co^{2+} d to d on-site transitions [28]. In addition, the electronic excitations above ~ 3.00 eV were attributed to the O $2p$ to Fe $3d$ charge transfer excitations. Ravindra *et al.* investigated the band gap of CFO thin films grown on (001) oriented $LaAlO_3$ and found expansion of band-gap with the reduction of film thickness, which was explained by the quantum size effect and misfit dislocations. They found the band gap values of 2.505, 2.556, and 2.615 eV, respectively, for 581, 363, and 58 Å thick films [29]. Holinsworth *et al.* observed indirect and direct band gaps of 1.2 and 2.7 eV, respectively, for CFO films grown on $MgAl_2O_4$ substrates [30]. Himcinschi *et al.* also observed indirect and direct band gaps of 1.42 and 1.95 eV, respectively, for CFO film grown on Nb doped $SrTiO_3$ from ellipsometry [31].

The optical properties of CFO nanoparticles is less explored and studied experimentally besides the potential applications in fields, for instance photo-magnetism and catalysis [8,32], wherein establishing a comprehensive understanding of optical properties is required for a better tuning and performance. Moreover, the size and shape of nanostructures play an important role on the optical properties. So far, there are very few reports on the effect of annealing time on the optical properties of CFO nanoparticles. This motivated us to study the simple synthesis and characterization of CFO nanoparticles with an emphasis on the effect of annealing time on the optical properties. Therefore, in this article, we present the study of optical properties of CFO nanoparticles successfully synthesized via a simple co-precipitation route and annealed at 500 °C for different durations.

2 Materials and methods

2.1 Materials

The synthesis of cobalt ferrite nanoparticles was carried out using commercially available reagents. All the chemicals, including the metal salts $CoCl_2 \cdot 6H_2O$ and $FeCl_3 \cdot 6H_2O$, starch, and ethanol were purchased from Sigma Aldrich. All the chemicals purchased were of analytical grade and were used as-received without any further purification.

2.2 Synthesis of $CoFe_2O_4$ nanoparticles

$CoFe_2O_4$ nanoparticles were synthesized by co-precipitation route using stoichiometric ratios of metal chlorides as precursors, water as solvent, and potato starch as a surfactant. In a typical synthesis, 10 mmol of $CoCl_2 \cdot 6H_2O$, 20 mmol of $FeCl_3 \cdot 6H_2O$, and 0.5 g of potato starch were dissolved in 150 ml of de-ionized water and magnetically stirred for 1 h at 500 rpm at room temperature. The precipitating agent, 50 ml of 3 M NaOH aqueous solution, was then added drop-wise until the pH reached above 11 about when the metal hydroxides started to precipitate. The mixture was heated to 90 °C and was subsequently refluxed at this temperature for 2 h with continuous magnetic stirring (~ 500 rpm). The reaction mixture was allowed to cool down naturally to room temperature and transferred to a 30 mL centrifuge tube together with de-ionized water. The de-emulsified mixture was then centrifuged at ~ 6000 rpm

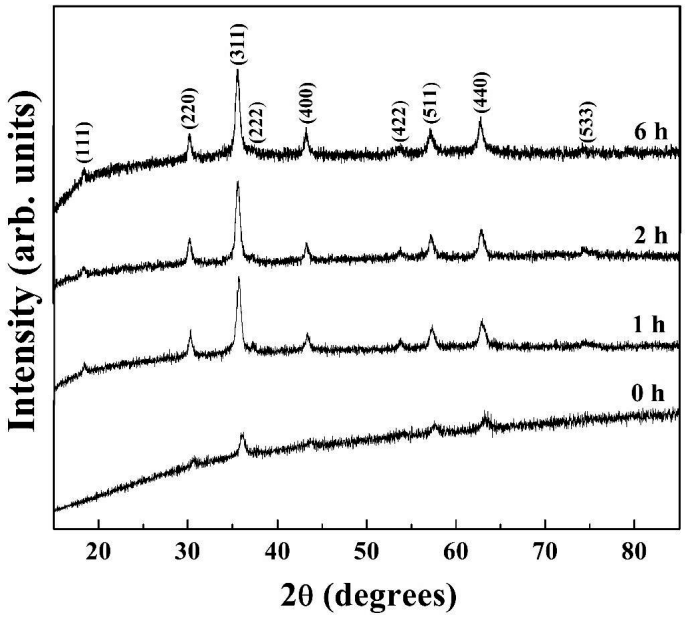

Fig. 1. X-ray diffraction patterns of as-synthesized and annealed (at 500 °C) $CoFe_2O_4$ nanoparticles for different durations.

for 15 min to isolate the supernatant liquid. The obtained precipitate was washed four times with de-ionized water and twice with ethanol to remove the salt contents present, centrifuged, and then dried at 90 °C for 12 h in a hot air oven to remove the excess ethanol and water. Further, the obtained co-precipitation product was annealed at 500 °C for different durations; 1, 2, and 6 h in air using high temperature furnace.

2.3 Characterizations

The phase of the as-synthesized and annealed co-precipitation products was examined using powder x-ray diffraction measurements performed on a Bruker D8 advance diffractometer employing Cu-K_α radiation ($\lambda = 1.5405$ Å) and Ni filtered, and the phase was confirmed by comparing the experimental powder x-ray diffraction patterns with the standard patterns compiled by the Joint Committee on Powder Diffraction and Standards (JCPDS). Distribution of cations at different sites within the structure is analyzed by performing Rietveld refinement with the help of GSAS suite equipped with EXPGUI software [33,34]. The shape, size, and chemical composition of the nanoparticles were analyzed by Field Emission Scanning Electron Microscope (ZEISS GeminiSEM 500). Fourier Transform Infrared (FTIR) spectra of characteristic peaks and functional group were recorded at room temperature on Bruker spectrometer in the range of 400–4000 cm^{-1} using KBr pellet technique. The absorbance spectra were recorded at room temperature using a dual-beam JASCO V-670 UV/VIS/NIR spectrophotometer in the wavelength range of 200–800 nm for evaluating the energy band gap. Room temperature photoluminescence emission (PL) and excitation (PLE) spectra were obtained using JASCO FP-8300 fluorescence spectrometer with a 150 W xenon lamp as excitation source.

3 Results and discussions

3.1 Structural studies

The powder x-ray diffraction patterns of the as-synthesized (0 h) co-precipitation product, and of the samples obtained by annealing the as-synthesized product at 500 °C for 1, 2, and 6 h are shown in fig. 1. The XRD patterns of all the samples display clear peaks corresponding to the (111), (220), (311), (222), (400), (422), (511), (440), and (533) Bragg's reflections of cubic spinel CFO phase with space group $Fd\bar{3}m$ (JCPDS card No. 89-1009). No additional peaks are observed in the XRD patterns, revealing the phase purity of the as-prepared and annealed CFO samples. In addition, the broad nature of the peaks is an indicative of the small particle size. The lattice parameter values calculated from the position of the fundamental (311) diffraction peak are presented in table 1, and it is found that the lattice parameter is smaller than that of the bulk CFO (8.412 Å) for all the samples [35]. It can be seen from table 1 that the lattice constant increases while the lattice strain decreases when annealed at 500 °C and for prolonged durations at the same temperature. The full width at half maximum (FWHM) decreases, at the same time, the peaks enhance, up on annealing the as synthesized co-precipitation product at 500 °C for 1 h. On further prolonging the annealing duration to 2 and 6 h, the FWHM of the main peak (311) continues to fall while the peak intensity increases. This

Table 1. The full width at half maximum (FWHM), crystallite size (D), lattice constant (a), and strain values of the as-synthesized and annealed CFO nanoparticles. *Strain $= ((a_{\text{bulk}} - a_{\text{nano}})/a_{\text{bulk}})$, where a_{bulk} is the lattice parameter of the bulk CFO and a_{nano} is the lattice parameter of the CFO nanoparticles under stress.

S. No.	Annealing time (h)	Crystallite size (nm)	FWHM (311)	Lattice parameter (Å)	*Strain (%)
1	0	16	0.570	8.255	1.633
2	1	19	0.476	8.354	0.690
3	2	20	0.471	8.365	0.562
4	6	24	0.441	8.378	0.408

Table 2. Atomic positions, Wyckoff sites, and cation distribution in CFO sample annealed at 500 °C for 6 h.

Elements	Wyckoff site	Symmetry	x	y	z
0.67Fe+0.33Co	$8a$	$-43m$	3/8	3/8	3/8
0.68Fe+0.32Co	$16d$	$-3m$	0	0	0
O	$32e$	$3m$	0.2431	0.2431	0.2431

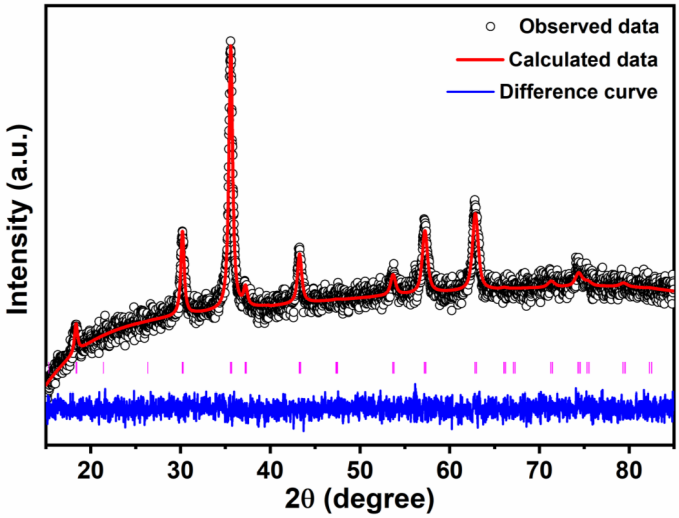

Fig. 2. Rietveld refinement plot of CFO sample annealed at 500 °C for 6 h.

indicates that, the crystallinity of CFO nanoparticles improves and the crystallites grow bigger in size leading to the increase of particle size, upon annealing at elevated temperature and also by prolonging the duration. The average crystallite size is estimated using Scherer formula and the values are presented in table 1. As anticipated, the average crystallite is the smallest (∼ 16 nm) for the as-synthesized product and it is the maximum (∼ 24 nm) for the sample annealed at 500 °C for 6 h. Therefore, the XRD of as-synthesized and annealed samples confirms the formation of pure spinel CFO phase with crystallite sizes in the nanometer scale.

As the crystallinity is increasing upon increasing the annealing duration, we carried out Rietveld refinement on the CFO sample that was annealed at 500 °C for 6 h. Through this refinement, the cation distribution at different sites was obtained. Structural information such as atomic positions and site occupancies of different atoms are summarized in table 2. It can be clearly seen from fig. 2 that the observed powder x-ray diffraction pattern clearly fits with cubic structure with $Fd\bar{3}m$ space group and the lattice parameter is turned out to be 8.375 Å. From the refinement results (see table 2) it is found that, $8a$ site is occupied by 67% of Fe and 33% of Co atoms whereas the site $16d$ is occupied with 68% Fe and 32% Co atoms. $32e$ site is fully occupied with oxygen atoms. The presence of Fe and Co in both the sites ($8a$ and $16d$) indicate the mixed spinel nature of CFO nanoparticles annealed at 500 °C for 6 h.

3.2 FTIR studies

The room temperature FTIR spectra of the as-synthesized (0 h) and annealed (at 500 °C for 1, 2, and 6 h) $CoFe_2O_4$ nanoparticles are shown in fig. 3. Generally, cubic ferrites exhibit two noticeable high frequency bands; ν_1 in the range 540–600 cm^{-1} and ν_2 in the range 400–450 cm^{-1}, corresponding to the vibrations of the metal ion-oxygen complexes in tetrahedral and octahedral sites, respectively [36,37]. The lower frequency band is sensitive to the cation occupancy in

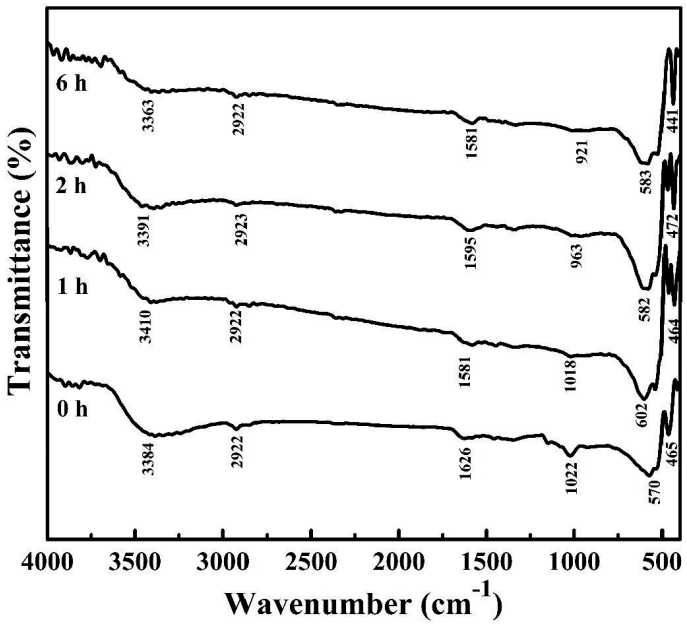

Fig. 3. FTIR spectra of as-synthesized and annealed (at 500 °C) $CoFe_2O_4$ nanoparticles for different durations.

octahedral site [38]. As can be seen from the FTIR spectra, all the samples demonstrate two strong peaks at around 465 and 570 cm^{-1}, characteristic of cubic ferrites, which are assigned to the vibrations of the metal ion-oxygen stretching vibrations in octahedral and tetrahedral sites, respectively [39,40]. It is observed that the intensity of the peak related to octahedral site increases when the annealing duration is raised from 1 to 6 h, indicating the cations preferring the octahedral sites than the tetrahedral sites at higher annealing duration [41]. At first, when annealed at 500 °C for 1 h, the metal-oxygen stretching vibrational peak blue shifts from 570 to 602 cm^{-1}, subsequently red shifts from 602 to 582 cm^{-1} when the annealing duration is prolonged to 2 and 6 h, which demonstrates the change in bond length with change of annealing time. A wide absorption in the high frequency region of the spectra at around 3300–3400 cm^{-1} is resulting from the -OH stretching of water molecules coordinated to the ferrite structure. The strength of this broad band decreases as annealing time increases due to the decrease of water content [41]. The band at $\sim$ 2922 cm^{-1} represents the C-H stretching and that at $\sim$ 1626 cm^{-1} is due to the C=O stretching. The peak observed in the range 900 to 1022 cm^{-1} is associated with the starch surfactant [35], and the shift in this peak with annealing time is an indicative of weakening of bonds due to reorganization of starch molecules after heat treatment [42]. The peak at $\sim$ 1022 cm^{-1} is attributed to the C-OH bond signifying the amorphous nature of starch [35], that at $\sim$ 963 cm^{-1} to =CH [43], and the peak at $\sim$ 921 cm^{-1} is ascribed to the CH_3 rocking vibration in starch [44]. The room temperature FTIR thus confirms the formation of cubic CFO phase and the successful embedding of the surfactant (starch).

3.3 SEM studies

Figure 4 shows the SEM images of as-synthesized and annealed $CoFe_2O_4$ nanoparticles. All the samples show nearly spherical morphology with no significant particle agglomeration, indicating the effective action of starch as the surfactant. The SEM image of as-synthesized sample (fig. 4(a)) shows distinct small particles of spherical morphology of average size $\sim$ 18–22 nm, whereas the average particle size is found to be $\sim$ 20–25, 24–29, and 32–39 nm for $CoFe_2O_4$ nanoparticles annealed at 500 °C for 1, 2, and 6 h, respectively (fig. 4(b)–(d)). The average particle sizes obtained from SEM analysis is greater than the corresponding average crystallite sizes calculated using Scherer formula (see table 1). The average particle size of the as-synthesized $CoFe_2O_4$ nanoparticles increases upon annealing at 500 °C, as well by prolonging the annealing time at the same temperature. In addition, the particle boundaries get indistinct when annealed at high temperature and for prolonged durations at the same temperature. This can be explained as follows; on heating at elevated temperatures and/or on prolonging the annealing durations at a constant temperature, the grain boundaries expand to merge together due to the removal of the organic surfactant from the sample leading to the increase of average particle size increases [41].

3.4 Band gap studies

To estimate the optical energy band gap of as-synthesized and annealed CFO nanoparticles, optical absorbance spectra were recorded at room temperature as given in fig. 5. The absorption spectra of as-synthesized and 1 h annealed CFO

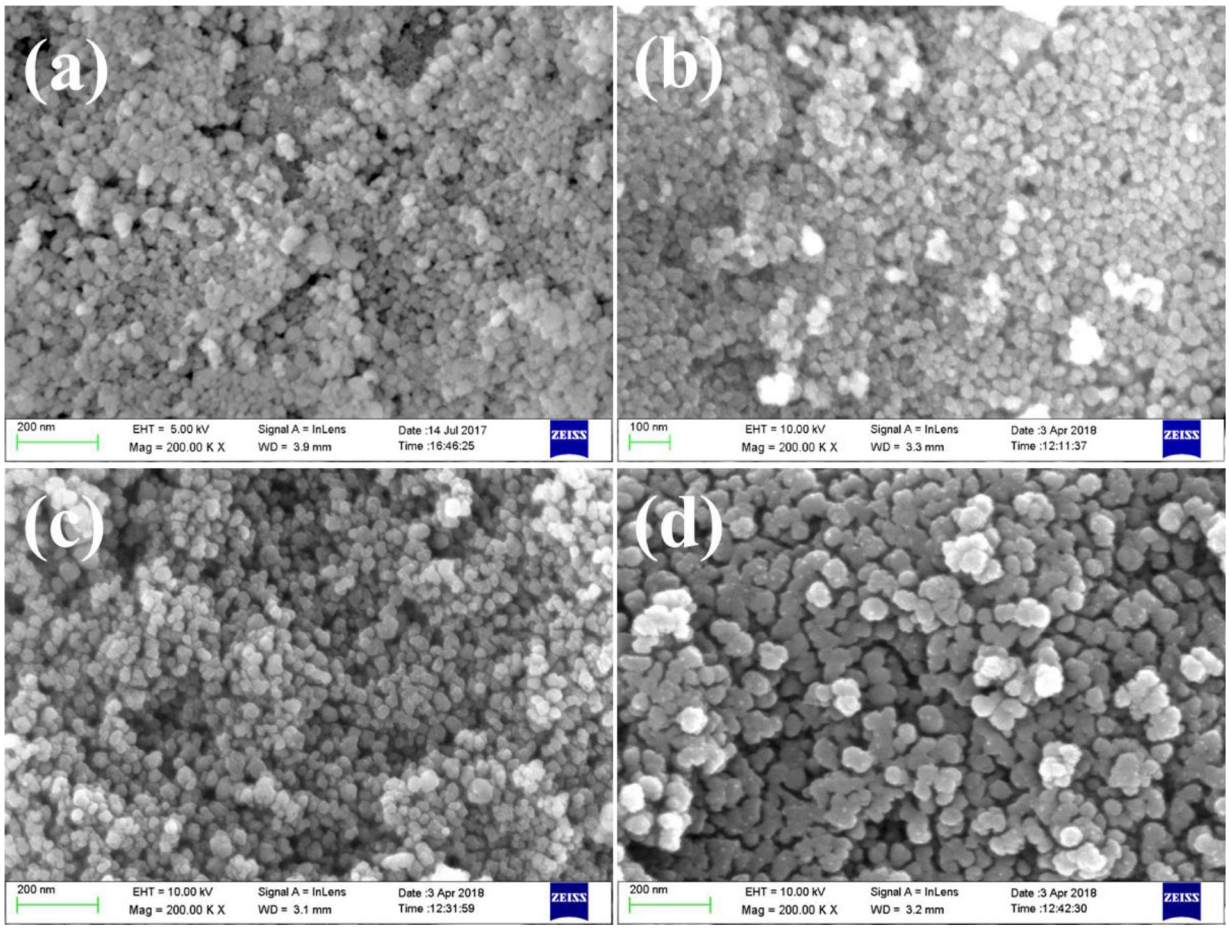

Fig. 4. SEM images of as-synthesized (a) and annealed $CoFe_2O_4$ nanoparticles ((b) 1 h, (c) 2 h, and (d) 6 h at 500 °C).

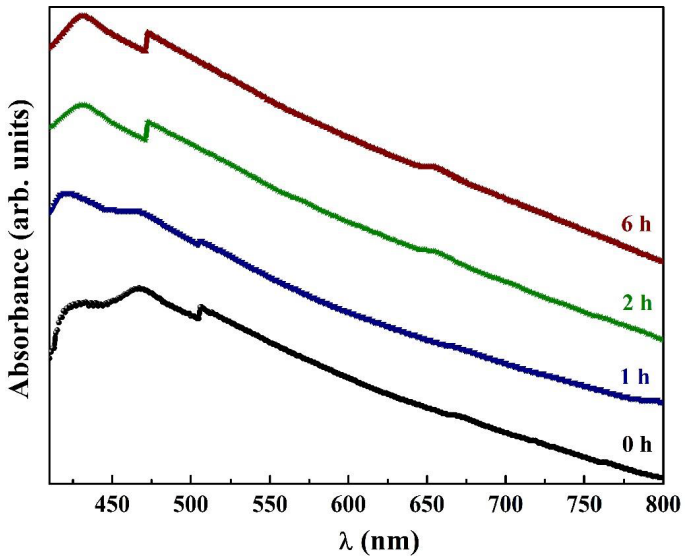

Fig. 5. Room temperature absorbance spectra of as-synthesized and annealed (at 500 °C) $CoFe_2O_4$ nanoparticles for different durations.

nanoparticles comprises of two peaks around 420 and 468 nm. In contrast, the CFO nanoparticles annealed at 500 °C for 2 and 6 h exhibit only one peak around 420 nm. These peaks can be attributed to the excitonic absorbance in these materials. The peak at 420 nm commonly observed for all the samples is attributed to the d-d transitions among Co^{2+} and Fe^{3+} ions and this would vary with temperature [45]. In addition, the variation of absorption peaks intensity can be due to the variation of the density of ions, which may lead to the change in the energy of the system [46].

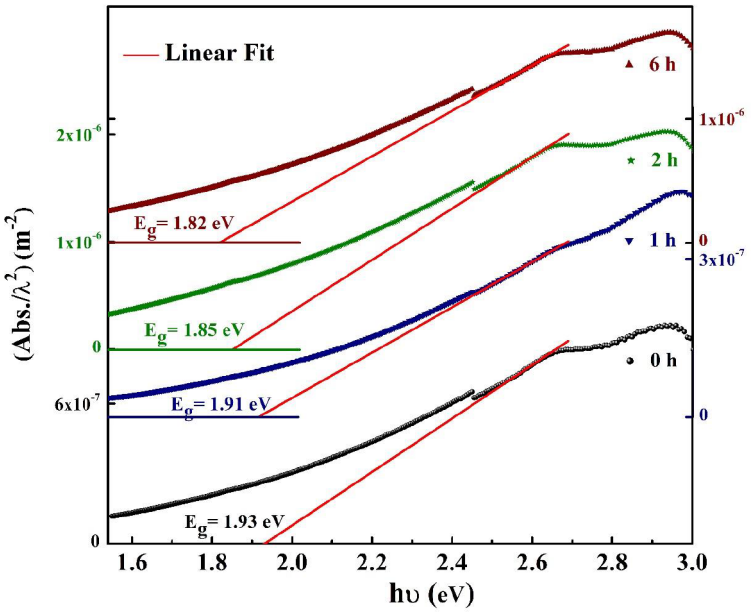

Fig. 6. Tauc plots of as-synthesized and annealed (at 500 °C) $CoFe_2O_4$ nanoparticles for different durations with a linear extrapolation of $(\frac{\text{Abs.}}{\lambda})^2$ to $h\nu = 0$.

In general, Tauc approach relating the absorption coefficient (α) to the incident photon energy ($h\nu$) in the expression; $\alpha h\nu = A(h\nu - E_g)^n$, where A is transition probability constant, h is Planck's constant, and n assumes the values $\frac{1}{2}$ for the allowed direct transition and 2 for the indirect allowed transition, $\frac{3}{2}$ for direct forbidden transition and 3 for indirect forbidden transition, is used to find the band gap (E_g) of nanoparticles. However, due to strong dependence of the absorption coefficient on the morphology of the nanostructures, its precise determination desires the uniform morphology of nanostructures. Therefore, we have modified the Tauc relation in terms of absorbance; $(\frac{\text{Abs.}}{\lambda})^2 = B(h\nu - E_g)^n$, where B is a constant related to A and morphology of nanostructures [47]. Therefore, to find the direct band gap of CFO nanoparticles $(\frac{\text{Abs.}}{\lambda})^2$ is plotted against $h\nu$, as shown in fig. 6. For all the samples, $(\frac{\text{Abs.}}{\lambda})^2$ varies linearly with $h\nu$ in the region of strong absorption near the fundamental absorption edge. The energy band gap is determined by extrapolating the linear part of $(\frac{\text{Abs.}}{\lambda})^2$ *vs.* $h\nu$ curve to $h\nu = 0$.

The direct band gap is found to be 1.93 eV for the as-synthesized CFO nanoparticles, while it is 1.91, 1.86, and 1.82 eV, respectively, for the CFO nanoparticles annealed at 500 °C for 1, 2, and 6 h. The obtained values of band gap of all the CFO nanoparticles are found to be more than the theoretical values; 0.8 eV [25], 0.72 eV [26], 0.63 eV [27], predicted for the bulk CFO. This expansion of band gap for CFO nanoparticles is attributed to the electron confinement at nano dimensions [48]. While the observed band gap values are close to that reported by Tanabe and Sugano. These band gap values are attributed to spin-allowed Co^{2+}, d to d on-site transition, $4T_{1g}(F) \rightarrow 4T_{1g}(P)$, as depicted in the energy level splitting of the Co^{2+} ($3d^7$) ion in an octahedral field [28]. Moreover, the low energy transitions below 3 eV in ferrites are generally attributed to spin-allowed but parity forbidden metal d to d on-site transitions that may arise due to the intrinsic local distortion of CoO_6 [49]. On the other hand, it is noticed that the band gap of CFO nanoparticles decreases when annealed at 500 °C and also by prolonging the duration at the same temperature. Note that the average size of CFO nanoparticles increases when annealed at 500 °C and also by prolonging the duration at the same temperature, seen from the SEM studies. Nevertheless, the band gap is affected by diverse factors such as the presence of impurities, structural parameters, and surface and interface effects [50,51].

3.5 PL studies

Photoluminescence (PL) spectroscopy is a useful technique to investigate energy as well as dynamics of charge carriers generated on light incidence and also to identify the nature and position of the emitting states. Further, PL spectroscopy can be used to study the defects and other impurity states of the material. Room temperature photoluminescence (PL) spectra of as-synthesized and annealed CFO nanoparticles recorded at $\lambda_{ex} = 465$ nm are shown in fig. 7. The emission spectra is observed in the visible and near IR range to study the energy changes associated with transitions of charge carriers to near edge, surface-, and defect-states in the material. In cubic spinel ferrites, electrons are present in trap states, exciton states and conduction bands [52]. In general, the defect states are the new donor levels created near the conduction band edge of the material which are the basis of luminescent properties in nanomaterials. Moreover, photoluminescence (PL) peaks may also be attributed to the recombination of charge carriers in deep traps of surface localized states and lattice defects [53,54].

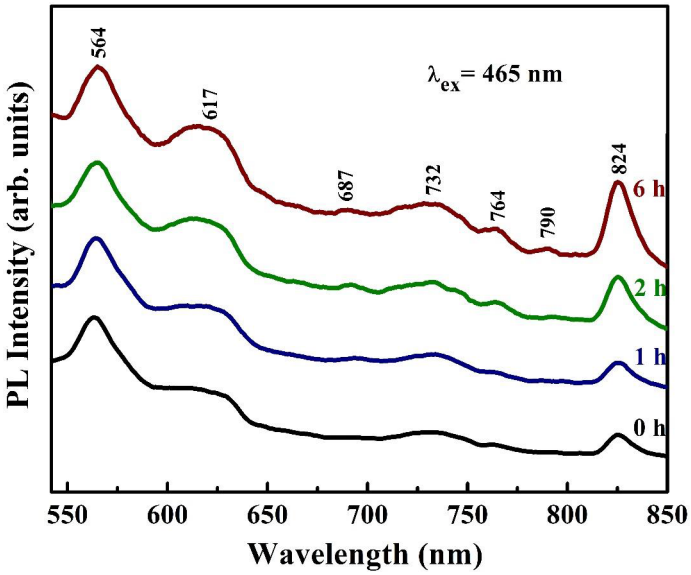

Fig. 7. Room temperature PL spectra of as-synthesized and annealed (at 500 °C) $CoFe_2O_4$ nanoparticles for different durations at excitation wavelength $\lambda_{ex} = 465$ nm.

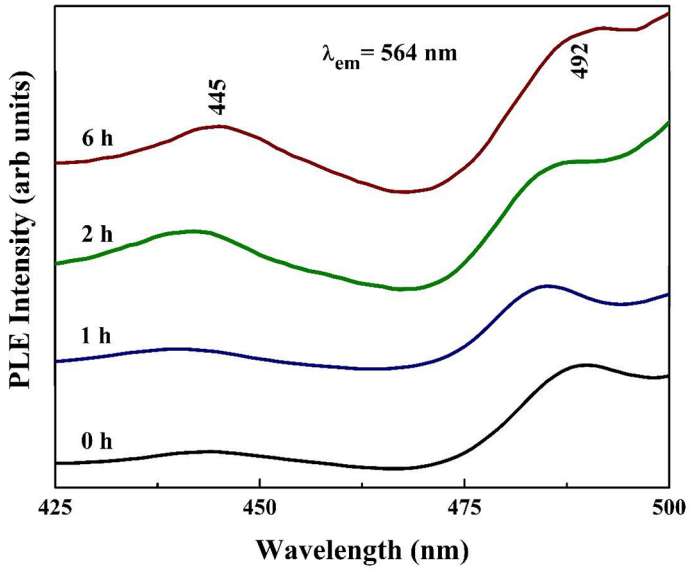

Fig. 8. Room temperature PLE spectra of as-synthesized and annealed (at 500 °C) $CoFe_2O_4$nanoparticles for different durations at emission wavelength $\lambda_{em} = 564$ nm.

The PL spectrum of as-synthesized CFO nanoparticles demonstrates five noticeable peaks; two strong and relatively sharp peaks centered at about ∼ 564 and ∼ 824 nm, a strong and relatively broad peak at about ∼ 617 nm along with a weak peak at about ∼ 764 nm. It can be seen from fig. 7 that these five peaks are also observed for the CFO nanoparticles annealed at 500 °C for different times. Noticeably, the broad orange emission at ∼ 617 nm becomes narrower and the other peaks intensities get improved when the annealing duration is prolonged at the same temperature, which can be attributed to the crystallinity improvement due to annealing [55]. However, in case of the CFO nanoparticles annealed at 500 °C for 1 h, a new peak appears at ∼ 687 nm, which gets pronounced by increasing the annealing time to 2 h at the same temperature. For the CFO nanoparticles annealed at 500 °C for 6 h, an additional weak peak evolves at ∼ 790 nm. The modification in peaks intensities can be attributed to the appearance of new electronic levels in the forbidden region that might result from the intrinsic defects [56]. In addition, substantial reduction of the energy levels in the band gap simultaneously decrease the recombination rate of electron-holes, leading to the variation of PL peaks intensity. The 824 nm peak, characteristic of the ferrite materials, is resulting of deep level oxygen induced transitions [57]. The emission spectra of CFO nanoparticles in the visible and near IR range is ascribed to the energy changes associated with transitions of charge carriers to near edge, surface-, and defect-states [52] in the material with change in annealing conditions.

The room temperature photoluminescence emission (PLE) spectra of as-synthesized and annealed CFO nanoparticles were recorded at the wavelength correspond to the emission peak at 564 nm as shown in fig. 8. Commonly, the PLE spectrum of all the CFO nanoparticles comprises of two peaks at around; 444 and 490 nm for as-synthesized, 440 and 485 nm for 1 h annealed, 442 and 486 nm for 2 h annealed, and 445 and 492 nm for 6 h annealed. The lower wavelength peak is not obvious for the as-prepared and annealed (500 °C for 1 h) CFO nanoparticles. Similar to PL peaks, PLE peaks also get intensified for higher annealing time. The PLE peaks exhibit blue shift when annealed at 500 °C for 1 h and then red shift on further prolonging the annealing time to 2 and 6 h at the same temperature.

4 Conclusions

In conclusion, $CoFe_2O_4$ nanoparticles were successfully synthesised by simple and economic co-precipitation method at 90 °C for 2 h using a biodegradable surfactant (starch), and by annealing at 500 °C for different durations. The spinel $CoFe_2O_4$ phase was clearly identified by x-ray diffraction for as-synthesized and annealed samples without any impurity phase. The room temperature FTIR spectra too displayed the characteristic absorption bands of $CoFe_2O_4$ and starch surfactant. SEM examination revealed spherical morphology of $CoFe_2O_4$ nanoparticles and the average particle size was found to increase by annealing at 500 °C and also by prolonging the annealing duration at the same temperature. The direct band gap of $CoFe_2O_4$ nanoparticles reduced with increasing particle size and the direct band gap values were attributed to spin-allowed d to d on-site transitions. The PL spectra showed peaks corresponding to the energy changes associated with transitions of charge carriers to near edge, surface-, and defect-states. The PLE peaks blue shifted when annealed at 500 °C for 1 h and then red shifted on further prolonging the annealing time to 2 and 6 h at the same temperature. The results of this study are expected to offer new opportunities for optimizing and enhancing the performance of cobalt ferrite where the optical properties play a key role.

AVR acknowledges the financial support provided by Yunnan Province Post-Doctoral Training Fund-2019 and Kunming University of Science and Technology for the Post-Doctoral Fellowship. MC would like to acknowledge the Department of Science and Technology for providing funding through DST-FIST Level-1 Scheme to Department of Physics, KLEF; File No: SR/FST/PS-1/2018/35. CR thanks the financial support provided by the Department of Science and Technology (DST-SERB) under the scheme of Young Scientist (File No: SB/FTP/ETA-0213/2014). The authors also thank Dr. K. Swapna and Dr. A. Venkateswara Rao for extending their lab facilities.

Author contribution statement

A.V. Ravindra and M. Chandrika contributed equally to this work.

Conflict of interest

The authors report no conflicts of interest. The authors alone are responsible for the content and writing of this article.

References

1. Q. Zhao, Z. Yan, C. Chen, J. Chen, Chem. Rev. **117**, 10121 (2017).
2. S. Jauhar, J. Kaur, A. Goyal, S. Singhal, RSC Adv. **6**, 97694 (2016).
3. O. Vozniuk, T. Tabanelli, N. Tanchoux, J.-M.M. Millet, S. Albonetti, F. Di Renzo, F. Cavani, Catalysts **8**, 332 (2018).
4. S.D. Raut, V.V. Awasarmol, B.G. Ghule, S.F. Shaikh, S.K. Gore, R.P. Sharma, P.P. Pawara, R.S. Mane, Mater. Res. Express **5**, 065035 (2018).
5. K.L. Routray, B. Sahoo, D. Behera, Mater. Res. Express **5**, 085016 (2018).
6. K. Benzid, D. Muller, P. Turek, J. Tribollet, Eur. Phys. J. B **88**, 58 (2015).
7. M.M. Ismail, S.N. Rafeeq, J.M.A. Sulaiman, A. Mandal, Appl. Phys. A **124**, 380 (2018).
8. A.K. Giri, E.M. Kirkpatrick, P. Moongkhamklang, S.A. Majetich, Appl. Phys. Lett. **80**, 2341 (2002).
9. S. Boumaza, A. Boudjemaa, A. Bouguelia, R. Bouarab, M. Trari, Appl. Energy **87**, 2230 (2010).
10. Y.S. Srinivasan, K.M. Paknikar, D. Bodas, V. Gajbhiye, Nanomedicine **10**, 1221 (2018).
11. S. Amiri, H. Shokrollahi, Mater. Sci. Eng. C **33**, 1 (2013).

12. A.V. Ramos, T.S. Santos, G.X. Miao, M.-J. Guittet, J.-B. Moussy, J.S. Moodera, Phys. Rev. B **78**, 180402(R) (2008).
13. V. Thakare, G. Xing, H. Peng, A. Rana, O. Game, P.A. Kumar, A. Banpurkar, Y. Kolekar, K. Ghosh, T. Wu, D.D. Sarma, S.B. Ogale, Appl. Phys. Lett. **100**, 172412 (2012).
14. R.V. Chopdekar, Y. Suzuki, Appl. Phys. Lett. **89**, 182506 (2006).
15. G.A. Sawatzky, F. Van Der Woude, A.H. Morrish, Phys. Rev. **187**, 747 (1969).
16. T.A.S. Ferreira, J.C. Waerenborgh, M.H.R.M. Mendonc, M.R. Nunes, F.M. Costa, Solid State Sci. **5**, 383 (2003).
17. Y. Zhang, Z. Yang, D. Yin, Y. Liu, C. Fei, R. Xiong, J. Shia, G. Yan, J. Magn. & Magn. Mater. **322**, 3470 (2010).
18. K. Maaz, A. Mumtaz, S.K. Hasanain, A. Ceylan, J. Magn. & Magn. Mater. **308**, 289 (2007).
19. T. Tatarchuk, M. Bououdina, J.J. Vijaya, L. John Kennedy, Springer Proc. Phys. **195**, 305 (2017).
20. B. Purnama, A.T. Wijayanta, Suharyana, J. King Saud Univ. - Sci. (2018) `https://doi.org/10.1016/j.jksus.2018.07.019`.
21. T.E. Alves, H.V. Pessoni, A. Franco Junior, Phys. Chem. Chem. Phys. **19**, 16395 (2017).
22. V. Mameli, A. Musinu, A. Ardu, G. Ennas, D. Peddis, D. Niznansky, C. Sangregorio, C. Innocenti, N.T.K. Thanh, C. Cannas, Nanoscale **8**, 10124 (2016).
23. A. Abu El-Fadl, A.M. Hassan, M.H. Mahmoud, T. Tatarchuk, I.P. Yaremiy, A.M. Gismelssed, M.A. Ahmed, J. Magn. & Magn. Mater. **471**, 192 (2019).
24. M.A. Ahmed, H.E. Hassan, M.M. Eltabey, K. Latka, T.R. Tatarchuk, Physica B: Phys. Condens Matter. **530**, 195 (2018).
25. Z. Szotek, W.M. Temmerman, D. Ködderitzsch, A. Svane, L. Petit, H. Winter, Phys. Rev. B **74**, 174431 (2006).
26. Y.H. Hou, Y.J. Zhao, Z.W. Liu, H.Y. Yu, X.C. Zhong, W.Q. Qiu, D.C. Zeng, L.S. Wen, J. Phys. D: Appl. Phys. **43**, 445003 (2010).
27. V.N. Antonov, B.N. Harmon, A.N. Yaresko, Phys. Rev. B **67**, 024417 (2003).
28. Y. Tanabe, S. Sugano, I. J. Phys. Soc. Jpn. **9**, 753 (1954).
29. A.V. Ravindra, P. Padhan, W. Prellier, Appl. Phys. Lett. **101**, 161902 (2012).
30. B.S. Holinsworth, D. Mazumdar, H. Sims, Q.-C. Sun, M.K. Yurtisigi, S.K. Sarker, A. Gupta, W.H. Butler, J.L. Musfeldt, Appl. Phys. Lett. **103**, 082406 (2013).
31. C. Himcinschi, I. Vrejoiu, G. Salvan, M. Fronk, A. Talkenberger, D.R.T. Zahn, D. Rafaja, J. Kortus, J. Appl. Phys. **113**, 084101 (2013).
32. M. Kazemi, M. Ghobadi, A. Mirzaie, Nanotechnol. Rev. **7**, 43 (2018).
33. A.C. Larson, R.B. von Dreele, General Structural Analysis System (GSAS), Los Alamos National Laboratories, Los Alamos, NM, 1990.
34. B.H. Toby, J. Appl. Crystallogr. **34**, 210 (2001).
35. J. Kazimierczak, D. Ciechańska, D. Wawro, K. Guzińska, Fibres Text. East. Eur. **15**, 100 (2007).
36. B.R. Babu, T. Tatarchuk, Mater. Chem. Phys. **207**, 534 (2018).
37. T.R. Tatarchuk, M. Bououdina, N.D. Paliychuk, I.P. Yaremiy, V.V. Moklyak, J. Alloys. Compd. **694**, 777 (2017).
38. J.L.M. De Vidales, A.L. Delgado, E. Vila, F.A. López, J. Alloys Compd. **287**, 276 (1999).
39. F.A. Lopez, D.A. Lopez, V.J.L. Martin de, E. Vila, J. Alloys. Compd. **265**, 291 (1998).
40. T.R. Tatarchuk, N.D. Paliychuk, M. Bououdina, B. Al-Najar, M. Pacia, W. Macyk, A. Shyichuk, J. Alloys. Compd. **731**, 1256 (2018).
41. B. Purnama, R. Rahmawati, A.T. Wijayanta, Suharyana, J. Magn. **20**, 207 (2015).
42. D.M. Kasote, M.D. Oak, S.S. Nilegaonkar, V.V. Agte, Int. Food Res. J. **25**, 1 (2018) issue No. 1.
43. P. Mani, S. Suresh, Rasayan J. Chem. **2**, 340 (2009).
44. K. Fukushima, Y. Kimura, Polym. Int. **55**, 626 (2006).
45. K.J. Kim, H.S. Lee, M.H. Lee, S.H. Le, J. Appl. Phys. **91**, 9974 (2002).
46. R.V. Pisarev, A.S. Moskvin, A.M. Kalashnikova, Th. Rasing, Phys. Rev. B **79**, 235128 (2009).
47. A.V. Ravindra, B.C. Behera, P. Padhan, J. Nanosci. Nanotechnol. **14**, 5591 (2014).
48. A.P. Alivisatos, Science **271**, 933 (1996).
49. R.C. Rai, S. Wilser, M. Guminiak, B. Cai, M.L. Nakarmi, Appl. Phys. A **106**, 207 (2012).
50. M.F.-Garcia, J.A. Rodriguez, *Metal Oxide Nanoparticles*, in Encyclopedia of Inorganic Chemistry (John Wiley & Sons, Ltd. New York, USA, 2011) pp. 1–3.
51. V.G. Andreeva, S.B. Menshovaa, A.Y. Kirinaa, S.B. Bibikovb, M.V. Prokofevc, V.M. Prokhorovd, Nanotechnol. Russ. **11**, 9 (2016).
52. D.E. Skinner, D.P. Colombo, J.J. Cavaleri, R.M. Bowman, J. Phys. Chem. **99**, 7853 (1995).
53. A. Sengupta, B. Jiang, K. Mandal, J. Zhang, J. Phys. Chem. B **103**, 3128 (1999).
54. U. Resch, A. Eychmuller, M. Hasse, H. Wellner, Langmuir **8**, 2215 (1992).
55. L. Kumar, M. Kar, IEEE Trans. Magn. **47**, 3645 (2011).
56. A. Manikandan, J.J. Vijaya, L.J. Kennedy, M. Bououdina, J. Mol. Struct. **1035**, 332 (2013).
57. D. Shi, M.E. Sadat, A.W. Dunn, D.B. Mast, Nanoscale **7**, 8209 (2015).